

TOWARDS NON-CONTACT MACROSCOPIC IMAGING OF MULTIPLE CANCERS USING MULTI-SPECTRAL INELASTIC SCATTERING DETECTION

SANDRYNE DAVID,^{1,2} NASSIM KSANTINI,^{1,2} FRÉDÉRIK DALLAIRE,^{1,2} KATHERINE EMBER,^{1,2} FRANÇOIS DAOUST,^{1,2} GUILLAUME SHEEHY,^{1,2} COSTAS G. HADJIPANAYIS,^{3,4} KEVIN PETRECCA,⁵ BRIAN C. WILSON,⁶ FRÉDÉRIC LEBLOND^{1,2,7,*}

¹DEPARTMENT OF ENGINEERING PHYSICS, POLYTECHNIQUE MONTRÉAL, MONTREAL, QUÉBEC, CANADA.

²Centre de Recherche du Centre Hospitalier de l'Université de Montréal (CRCHUM), Montréal, Quebec, Canada

³Mount Sinai Hospital, New York, NY, USA

⁴University of Pittsburgh Medical Center, Pittsburgh, PA, USA

⁵Montreal Neurological Institute-Hospital, McGill University, Montreal, Canada

⁶Princess Margaret Cancer Center-University Health Network/University of Toronto, Toronto, Ontario, Canada

⁷Institut du cancer de Montréal, Montreal, Quebec, Canada

*Frederic.leblond@polymtl.ca

Received XX Month XXXX; revised XX Month, XXXX; accepted XX Month XXXX; posted XX Month XXXX (Doc. ID XXXXX); published XX Month XXXX

***In situ* spontaneous Raman spectroscopy at sub-millimeter detection scales has been reported previously to guide tumor resection. However, single-point spectroscopy is limited in its ability to sample whole surgical margins rapidly and avoid under-sampling. A retrospective analysis of Raman spectroscopy datasets acquired on four cancer types has shown that the spectral bands around 1004, 1302, 1440, and 1657 cm⁻¹ were common cancer biomarkers. Linear SVM classification models were developed to detect cancer with only 3 spectral bands and showed a sensibility and specificity close to the one obtained with the original classification. These results led to the development of a multi-spectral imaging system that has the capability to map a Raman biomarker, over a >2 cm² field-of-view. A proof-of-principle study is presented imaging the wavenumber band centered at 1440 cm⁻¹ associated lipids and proteins in porcine tissues. Wide-field single-band imaging was achieved in ~5 seconds and preliminarily demonstrated the identification of distinct tissue regions. This study paves the way for the development of a new Raman imaging technique that is rapid, label-free, and wide-field.**

Recent advances have shown *in situ* single-point intraoperative measurements at millimeter scales can be achieved within a few seconds [1,2]. To date, practical intraoperative Raman spectroscopy applications were developed mostly using single-point detection mode. Those included brain tumor surgery guidance [3], bronchoscopy [4], colorectal endoscopy [5], skin lesion screening [6], breast cancer surgery [7,8], and prostate biopsy guidance [9]. If attainable, *in vivo* wide-field Raman imaging at macroscopic scales (centimeter-size field-of-view) could complement, and possibly even replace, *in vivo* imaging of fluorescence markers, including indocyanine green [10] and fluorescein [11]. However, achieving wide-field Raman imaging on par with fluorescence molecular imaging would, in principle, require one spectrum to be detected in every imaged pixel. This is simply not practical since *whole* Raman spectra typically comprise hundreds of individual spectral bins, leading to imaging times of several minutes even for a modest –sub-centimeter-size– field-of-

view. For example, our group developed a hyperspectral line-scanning system that imaged adipose-muscle tissue margins in porcine specimens in less than 5 minutes across a 1 cm² field-of-view [12]. Clinical studies with that system demonstrated high accuracy pixelized cancer detection could be achieved in invasive breast carcinoma [13] within timescales of the order of 15 minutes. This makes these techniques –although highly sensitive and specific to cancer– more appropriate for *ex vivo* intraoperative margins assessment than for live surgical guidance.

The prospect of detecting inelastic scattering contrast *in vivo* in real-time remains enticing. However, this could only be feasible if tumor tissue detection did not require *whole* spectra to be acquired, but rather only a subset of Raman biomarkers. To assess the potential use of a subset of spectral features for cancer detection, we performed a retrospective analysis of four published tissue datasets from our group where a single-point Raman spectroscopy

instrument was used. One dataset was from a multicentric study where *in vivo* brain tumor Raman spectra were acquired (glioblastoma, meningioma, metastases) in 67 patients undergoing surgery (565 spectra in cancer, 420 in normal brain) [14]. The three other studies included spectra acquired with the same type of instrument albeit *ex vivo* in tissue specimens: 20 invasive breast cancer patients (87 spectra in cancer, 151 in normal breast tissue structures [7], 10 lung cancer patients (97 spectra in cancer, 100 in normal lung tissue [15], 9 patients with either ovarian or endometrial cancer (28 spectra in cancer, 42 in normal tissue) [16]. The machine learning cancer detection models published for each application had sensitivity/specificity of 87%/95% for brain, 93%/95% for breast, 94%/80% for lung, and 93%/88% for ovarian/endometrium (Table 1).

Spectra for all datasets were pre-processed, including dark noise correction, *x*-axis wavenumber calibration, *y*-axis calibration correction (instrument response function normalization), removal of cosmic rays and non-Raman background (e.g., endogenous tissue fluorescence), and Standard Normal Variate (SNV) normalization [17]. Based on our experience with human tissue Raman spectra, 7 spectral regions were selected that had both a clear biomolecular interpretation and contained either one or two visually distinguishable peaks. For each feature, a spectral band of width ranging from 10 cm^{-1} to 15 cm^{-1} was selected.

A receiver-operating-characteristic (ROC) analysis was performed for each of the 7 spectral features, establishing its individual tumor detection potential. The sensitivity/specificity and the area-under-the-curve (AUC) of the ROC curve were reported for the four bands associated with the highest performance characteristics (Table 1). Two bands were common to all cancer types: I) the spectral band centered at 1440 cm^{-1} that is associated with the overlapping of several lipids (CH_2 and CH_3 bend and deformation) [18] and proteins (C-H) [19], II) the spectral band centred at 1004 cm^{-1} that is usually assigned with phenylalanine [19]. The spectral band centered at 1657 cm^{-1} , associated with lipids (C=C stretch) and proteins (Amid I) [18,19], was a strong biomarker for lung cancer and ovarian/endometrial cancer, but not for brain and breast cancer. The spectral band centered at 1302 cm^{-1} , associated with lipids (saturated bonds CH_2 and C-H vibration) as well as the amide III of proteins [18–20], was an effective biomarker for brain and breast cancer, but not for lung and ovarian/endometrial cancer.

Following the analysis based on individual Raman bands, a more complex support vector machines (SVM) model was trained and validated –for each cancer type– using only the three bands with the most predictive power. This led to a sensitivity/specificity (AUC) of 82%/91% (0.90) for brain, 92%/91% (0.96) for breast, 94%/80% (0.84) for lung, and 93%/85% (0.90) for ovarian/endometrium (Table 1). The quantitative similarity of those results with those already published –relying on automated spectral features extraction (dimensional reduction) and SVM modeling based on <15 features [16]– demonstrates that there exist Raman cancer biomarkers common to different cancer types. This puts in sharp focus the fact *whole* spectra may not always be required when developing Raman-based biomedical tissue optics applications. However, this finding can only be of practical relevance if methods are developed allowing individual bands to be isolated/detected without the requirement for *whole* spectra to be acquired. No such

technique exists and current numeric methods rely on curve fitting approaches to isolate low-frequency (in cm^{-1} space) contributions (i.e., fluorescence background) from the Raman signal of interest that is associated with higher frequency contributions [21].

Table 1. Detection of four cancer types (brain, breast, lung, ovarian/endometrium) using spectral features associated with inelastic scattering spectra acquired in tissue with a single-point Raman spectroscopy system. The reported results are associated with ROC curve analyses from which the area-under-the-curve (AUC), the Sensitivity (Sens) and the Specificity (Spec) were computed.

Model/ Features	Brain Sens/Spec (AUC)	Breast Sens/Spec (AUC)	Lung Sens/Spec (AUC)	Ovarian/ endometrium Sens/Spec (AUC)
SVM (<15 features)	87/95 % (0.94) [14]	93/95 % (0.98) [7]	94/80 % (0.83) [15]	93/88 % (0.96) [16]
Single band 1440 cm^{-1}	86/77 % (0.86)	89/70 % (0.82)	90/67 % (0.81)	93/46 % (0.50)
Single band 1004 cm^{-1}	73/87 % (0.86)	82/96 % (0.96)	76/50 % (0.60)	78/52 % (0.62)
Single band 1657 cm^{-1}	-	-	95/79 % (0.88)	56/93 % (0.85)
Single band 1302 cm^{-1}	75/72 % (0.77)	83/69 % (0.78)	-	-
SVM 3-bands	82/91 % (0.90)	92/91 % (0.96)	94/80 % (0.84)	93/85 % (0.90)

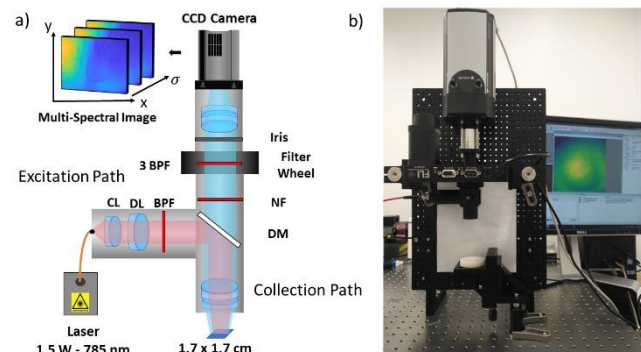


Fig. 1. Experimental setup allowing multi-spectral detection of inelastic scattering in biological tissue: a) Schematic representation comprising epi-illumination through an excitation path formed by an optical fiber, a collimating lens (CL), a band-pass filter (BPF), a diverging lens, a dichroic mirror (DM) and a focusing lens. The light collection path includes a notch filter (NF), a filter wheel with 9 interference bandpass filters, and a CCD camera. All lenses are spherical except LH (cylindrical with curvature in the horizontal direction) and LV (cylindrical lenses with curvature in the vertical direction); b) photograph of the system demonstrating simplicity of implementation.

Here, we present –for the first time– a proof-of-principle study demonstrating that an epi-illumination multi-spectral imaging system can be used to image individual Raman bands macroscopically over a large field-of-view (Fig. 1). Specifically, we demonstrate that the inelastic scattering signal from the band around 1440 cm^{-1} can be isolated from background fluorescence from images acquired at only 3 wavelengths. The system comprises a 1.5 W wavelength-stabilized 785 nm laser (Innovative Photonic Solutions, NJ, USA) with < 2 nm bandwidth. The light source is coupled to a 1,500 μm core 0.5 NA (numerical aperture) optical

fiber. The light from the fiber passes through a beam-expander lens, a collimation lens, an optical density (OD) 6 bandpass filter with central wavelength 785 nm and 167 nm bandwidth (Semrock, NY, USA), a dichroic mirror, and, finally, a lens allowing to control the beam spot size on the specimen. Back-scattered light is collected through the same focusing lens and the dichroic mirror prior to detection through an OD 6 high-pass filter with >785 nm cut-off (ThorLabs, NJ, USA), a motorized filter wheel (Finger Lakes Instrumentation, NY, USA) that can hold up to 9 band-pass filters and a CCD camera (Andor IKON M, Oxford Instruments, MA, USA). The camera has 1024 x 1024 pixels of 13 μm width, 5 MHz pixel readout and it was cooled to -64°C. The filters were selected to ensure that the band around 1440 cm^{-1} could be resolved, including minima to the left and right of the peak. Specifically, three OD 6 band-pass interference filters with 0.8 nm bandwidth were used with central wavelengths corresponding to wavenumber shifts (from 785 nm) of 1407, 1440 and 1492 cm^{-1} . The 2.1 cm^2 field-of-view comprised, after 16x16 binning to decrease photonic noise, 64x64 pixels with a spatial resolution of 225 μm .

Four porcine specimens were imaged that had a 1 cm thickness with grossly flat faces and a visually detectable margin between adipose and muscle tissue. Both the multi-spectral system and the line-scanning hyperspectral Raman system were independently used to acquire images of the same region-of-interest [12]. The hyperspectral images were considered the gold standard to be used as validation for the Raman biomarker images produced with the multi-spectral system. The hyperspectral system had a field-of-view of 1 cm^2 with 40 x 37 pixels, a spatial resolution of 250 μm and a spectral resolution of 6 cm^{-1} . The tissue specimens were placed onto an Aluminum surface to minimize inelastic scattering background interference. Images were acquired over a region that showed a distinct margin between adipose and muscle tissue. Figure 2 shows, for one of the four specimens, the raw (Fig. 2a) and processed SNV-normalized spectra (Fig. 2b) averaged over the whole image, along with the standard deviation for each spectral bin. The bandpass filters selected to be included in the wheel of the multi-spectral system were centered at $\sigma_1 = 1407 \text{ cm}^{-1}$, $\sigma_3 = 1492 \text{ cm}^{-1}$ (minimum Raman activity) and $\sigma_2 = 1440 \text{ cm}^{-1}$.

A measurement with the multi-spectral system consisted of images at all 3 wavenumbers σ_i , $i = 1, 2, 3$. Each measurement was labeled $I_{\text{raw}}(x, y, \sigma_i)$, where x and y correspond to spatial coordinates on the specimen. The total imaging time was approximately 5 s for all bands. Dark noise measurements (laser turned off), labeled $B(x, y, \sigma_i)$, were also made for each wavenumber. Two other imaging sequences were made for calibration of the spatial and spectral responses of the instrument. The spatial response was determined using a Nylon-66 sample with high spatial uniformity (labeled $E_{x,y}(x, y, \sigma_i)$), while the spectral response calibration utilized a NIST SRM 2214 Raman calibration standard (labeled $E_{\sigma}(\sigma_i)$), imaging at each wavenumber and computing an average intensity value across the image. The spectral response, $E_{\sigma}(\sigma_i)$, was then computed by dividing the resulting scalar intensity value at each wavenumber by the value with the NIST standard.

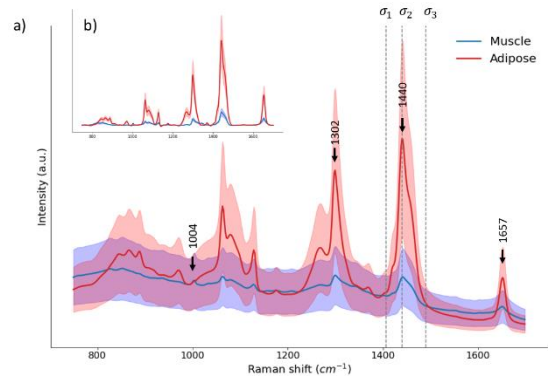


Fig. 2. Adipose and muscle tissue spectra acquired with the hyperspectral imaging system: a) Average raw spectrum and variance across the images; b) Same but for processed spectra after background removal. The vertical dotted lines in a) correspond to the three spectral bands used in the multi-spectral system at wavenumber shifts of 1407, 1440 and 1492 cm^{-1} . Dark arrows indicated the spectral bands used in the 3-bands models reported in Table 1.

Measurements acquired with the multi-spectral system can be modeled using the equation:

$$I_{\text{raw}}(x, y, \sigma_i) = E_{xy}(x, y, \sigma_i) \cdot E_{\sigma}(\sigma_i) \cdot [B(x, y, \sigma_i) + I(x, y, \sigma_i)] \quad (1)$$

where the quantity

$$I(x, y, \sigma_i) = D(x, y, \sigma_i) + R(x, y, \sigma_i) \quad (2)$$

is the sum of inelastic scattering, $R(x, y, \sigma_i)$, and background, $D(x, y, \sigma_i)$, that includes the endogenous tissue fluorescence. Isolating $I(x, y, \sigma_i)$ at each measured wavenumber was then achieved by normalizing the raw images by the Nylon and the NIST measurements.

In Raman spectroscopy, disentangling inelastic scattering from other background sources relies on acquiring *whole* spectra, followed by applying a curve-fitting algorithm to remove low-frequency contributions (in wavenumber space) [17,22] (Fig. 2). This has the effect of isolating the higher frequency information associated with the molecular vibrational bonds. By comparison, in multi-spectral Raman spectroscopy, we propose to isolate inelastic scattering through direct subtraction of the background contributions measured away from the Raman band of interest. Here, this was achieved by applying the following formula to retrieve the inelastic scattering contribution at 1440 cm^{-1} under the hypothesis that the off-band Raman contributions are negligible at $\sigma_1 = 1407 \text{ cm}^{-1}$ and $\sigma_3 = 1492 \text{ cm}^{-1}$:

$$R(x, y, 1440 \text{ cm}^{-1}) = I(x, y, 1440 \text{ cm}^{-1}) - \frac{[I(x, y, 1492 \text{ cm}^{-1}) - I(x, y, 1407 \text{ cm}^{-1})]}{2} \quad (3)$$

Figure 3 shows the results for one tissue specimen obtained with both imaging systems: See Supplemental material (Figures S1-S3) for the other specimens. The corresponding white-light images for the hyperspectral system (Fig. 3a) and the multi-spectral system (Fig. 3b) both show the same adipose-muscle margin. Images are also shown representing the raw intensity at 1440 cm^{-1} for the hyperspectral (Fig. 3c) and multi-spectral (Fig. 3d) systems, after dark-noise subtraction as well as spatial and spectral calibrations.

Fluorescence background removal was then applied to those images. For the hyperspectral system, this was achieved by applying the custom algorithm *BubbleFill* to every spectrum within the image (Fig. 3e) [17], and for the multi-spectral system by applying Eq. (3) (Fig 3f)). All images were normalized to their maximum value, with a color scale ranging from 0 to 1 to allow direct comparison of the detection contrast.

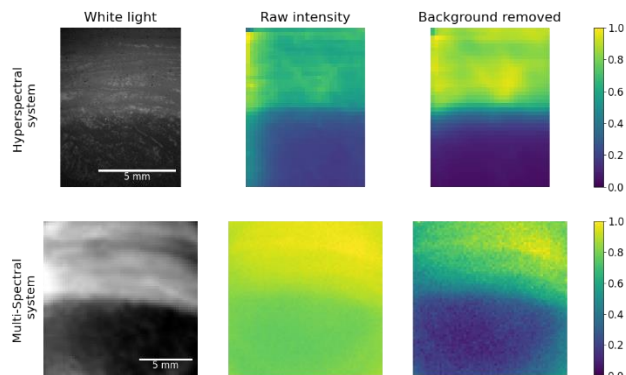


Fig. 3 Porcine tissue specimen images showing the margin between adipose and muscle tissue. (a,b) White-light images acquired with the hyperspectral and multi-spectral imaging systems. (c,d) Corresponding raw Raman signal intensity images (no background subtraction) in the 1440 cm^{-1} band. (e,f) Corresponding processed images following background removal. The two systems had a different fields-of-view but otherwise approximately represent the same area on the specimen. All images are normalized to their maximum value for direct comparison of the contrast associated with both modalities.

The resulting images for all specimens showed contrast levels at the adipose/muscle margin for the 1440 cm^{-1} biomarker that were consistent between the two imaging systems, demonstrating the ability of the multi-spectral system to isolate the inelastic scattering component associated with a single Raman band.

Being able to image the 1440 cm^{-1} biomarker has shown great potential for cancer detection as it yielded, by itself, ROC curves with an AUC above 0.80 for brain cancer, breast cancer and lung cancer. Two additional spectral bands could easily be imaged without any change to the system since the filter wheel can hold up to 9 filters. This would theoretically allow for the use of 3-band classification model to be used for cancer detection consistent with the bands presented in Table 1.

These results are preliminary, and more work should be done to demonstrate the capacity of the system to image cancer, however this work shows the potential for the next generation of Raman-based surgical guidance systems to in the form of rapid multi- or even single-band wide-field imaging. Combined with the finding of common Raman biomarkers of cancer, this could open the door for generalizable cancer imaging tools based on inelastic scattering.

Funding. This work is supported by Reveal Surgical, the Natural Sciences and Engineering Research Council of Canada (NSERC) Alliance grant program, the NSERC Discovery Grant program and the TransMedTech Institute

Disclosures. No Disclosures.

Data availability. The data and materials supporting the findings of this study are available from the corresponding author upon reasonable request.

References

1. M. Jermyn, K. Mok, J. Mercier, J. Desroches, J. Pichette, K. Saint-Arnaud, L. Bernstein, M. C. Guiot, K. Petrecca, and F. Leblond, *Sci. Transl. Med.* (2015).
2. K. Lin, J. Wang, W. Zheng, K. Y. Ho, M. Teh, K. G. Yeoh, and Z. Huang, *Cancer Prev. Res.* **9**, 476–483 (2016).
3. M. Jermyn, J. Mercier, K. Aubertin, J. Desroches, K. Urme, J. Karamchandani, E. Marple, M. C. Guiot, F. Leblond, and K. Petrecca, *Cancer Res.* (2017).
4. H. C. McGregor, M. A. Short, A. McWilliams, T. Shaipanich, D. N. Ionescu, J. Zhao, W. Wang, G. Chen, S. Lam, and H. Zeng, *J. Biophotonics* **10**, 98–110 (2017).
5. B. Brozek-Pluska, K. Miazek, J. Musiał, and R. Kordek, *RSC Adv.* **9**, 40445–40454 (2019).
6. N. Kourkouvelis, I. Balatsoukas, V. Moulia, A. Elka, G. Gaitanis, and I. D. Bassukas, *Int. J. Mol. Sci.* **16**, 14554–14570 (2015).
7. S. David, T. Trang, F. Dallaire, G. Sheehy, F. Azzi, D. Trudel, F. Tremblay, A. Omeroglu, F. Leblond, and S. Meterissian, *J. Biomed. Opt.* **29**, 1–33 (2023).
8. A. S. Haka, Z. Volynskaya, J. A. Gardecki, J. Nazemi, J. Lyons, D. Hicks, M. Fitzmaurice, R. R. Dasari, J. P. Crowe, and M. S. Feld, *Opt. Lett.* **31**, 3317–3323 (2006).
9. P. Crow, N. Stone, C. A. Kendall, J. S. Uff, J. A. M. Farmer, H. Barr, and M. P. J. Wright, *Br. J. Cancer* **89**, 106–108 (2003).
10. C. W. Teng, V. Huang, G. R. Arguelles, C. Zhou, S. S. Cho, S. Harmsen, and J. Y. K. Lee, *Neurosurg. Focus* **50**, 1–10 (2021).
11. A. V. Save, B. J. Gill, R. S. D’Amico, P. Canoll, and J. N. Bruce, *J. Neurosurg. Sci.* **63**, 648–655 (2019).
12. F. Daoust, T. Nguyen, P. Orsini, J. Bismuth, M.-M. de Denus-Baillargeon, I. Veilleux, A. Wetter, P. Mckoy, I. Dicaire, M. Massabki, K. Petrecca, and F. Leblond, *J. Biomed. Opt.* **26**, 1–18 (2021).
13. S. David, H. Tavera, T. Trang, F. Dallaire, F. Daoust, F. Tremblay, L. Richer, S. Meterissian, and F. Leblond, *J. Biomed. Opt.* **under rev**, (2023).
14. K. Ember, F. Dallaire, A. Plante, G. Sheehy, M.-C. Guiot, R. Agarwal, R. Yadav, A. Douet, J. Selb, J. Tremblay, A. Dupuis, E. Marple, K. Urme, C. Rizea, F. Leblond, C. G. Hadjipanayis, and K. Petrecca, *Nat. Commun.* **under rev**, (2023).
15. F. Leblond, F. Dallaire, T. Tran, R. Yadav, K. Aubertin, E. Goudie, P. Romeo, C. Kent, C. Leduc, and M. Liberman, *J. Biomed. Opt.* **28**, 1–8 (2023).
16. S. David, A. Plante, F. Dallaire, J. P. Tremblay, G. Sheehy, E. Macdonald, L. Forrest, M. Daneshmand, D. Trudel, B. C. Wilson, L. Hopkins, S. Murugkar, B. Vanderhyden, and F. Leblond, *J. Biophotonics* **15**, 1–10 (2022).
17. G. Sheehy, F. Picot, F. Dallaire, K. Ember, T. Nguyen, K. Petrecca, D. Trudel, and F. Leblond, *J. Biomed. Opt.* **28**, 1–20 (2023).
18. K. Czamara, K. Majzner, M. Z. Pacia, K. Kochan, A. Kaczor, and M. Baranska, *J. Raman Spectrosc.* **46**, 4–20 (2015).
19. A. Rygula, K. Majzner, K. M. Marzec, A. Kaczor, M. Pilarczyk, and M. Baranska, *J. Raman Spectrosc.* **44**, 1061–1076 (2013).
20. A. C. S. Talari, Z. Movasaghi, S. Rehman, and I. U. Rehman, *Appl. Spectrosc. Rev.* **50**, 46–111 (2015).
21. D. Wei, S. Chen, and Q. Liu, *Appl. Spectrosc. Rev.* (2015).
22. J. Zhao, H. Lui, D. I. Mclean, and H. Zeng, *Appl. Spectrosc.* **61**, 1225–1232 (2007).

Complete References

1. M. Jermyn, K. Mok, J. Mercier, J. Desroches, J. Pichette, K. Saint-

- Arnaud, L. Bernstein, M. C. Guiot, K. Petrecca, and F. Leblond, "Intraoperative brain cancer detection with Raman spectroscopy in humans," *Sci. Transl. Med.* (2015).
2. K. Lin, J. Wang, W. Zheng, K. Y. Ho, M. Teh, K. G. Yeoh, and Z. Huang, "Rapid fiber-optic raman spectroscopy for real-time in vivo detection of gastric intestinal metaplasia during clinical gastroscopy," *Cancer Prev. Res.* **9**, 476–483 (2016).
3. M. Jermyn, J. Mercier, K. Aubertin, J. Desroches, K. Urmey, J. Karamchandiani, E. Marple, M. C. Guiot, F. Leblond, and K. Petrecca, "Highly accurate detection of cancer in situ with intraoperative, label-free, multimodal optical spectroscopy," *Cancer Res.* (2017).
4. H. C. McGregor, M. A. Short, A. McWilliams, T. Shaipanich, D. N. Ionescu, J. Zhao, W. Wang, G. Chen, S. Lam, and H. Zeng, "Real-time endoscopic Raman spectroscopy for in vivo early lung cancer detection," *J. Biophotonics* **10**, 98–110 (2017).
5. B. Brozek-Pluska, K. Miazek, J. Musiał, and R. Kordek, "Label-free diagnostics and cancer surgery Raman spectra guidance for the human colon at different excitation wavelengths," *RSC Adv.* **9**, 40445–40454 (2019).
6. N. Kourkoumelis, I. Balatsoukas, V. Moulia, A. Elka, G. Gaitanis, and I. D. Bassukas, "Advances in the in vivo Raman spectroscopy of malignant skin tumors using portable instrumentation," *Int. J. Mol. Sci.* **16**, 14554–14570 (2015).
7. S. David, T. Trang, F. Dallaire, G. Sheehy, F. Azzi, D. Trudel, F. Tremblay, A. Omeroglu, F. Leblond, and S. Meterissian, "In situ Raman spectroscopy and machine learning unveil biomolecular alterations in invasive breast cancer," *J. Biomed. Opt.* **29**, 1–33 (2023).
8. A. S. Haka, Z. Volynskaya, J. A. Gardecki, J. Nazemi, J. Lyons, D. Hicks, M. Fitzmaurice, R. R. Dasari, J. P. Crowe, and M. S. Feld, "In vivo Margin Assessment during Partial Mastectomy Breast Surgery Using Raman Spectroscopy," 3317–3323 (2006).
9. P. Crow, N. Stone, C. A. Kendall, J. S. Uff, J. A. M. Farmer, H. Barr, and M. P. J. Wright, "The use of Raman spectroscopy to identify and grade prostatic adenocarcinoma in vitro," *Br. J. Cancer* **89**, 106–108 (2003).
10. C. W. Teng, V. Huang, G. R. Arguelles, C. Zhou, S. S. Cho, S. Harmsen, and J. Y. K. Lee, "Applications of indocyanine green in brain tumor surgery: review of clinical evidence and emerging technologies," *Neurosurg. Focus* **50**, 1–10 (2021).
11. A. V. Save, B. J. Gill, R. S. D'amico, P. Canoll, and J. N. Bruce, "Fluorescein-guided resection of gliomas.," *J. Neurosurg. Sci.* **63**, 648–655 (2019).
12. F. Daoust, T. Nguyen, P. Orsini, J. Bismuth, M.-M. de Denus-Baillargeon, I. Veilleux, A. Wetter, P. Mckoy, I. Dicaire, M. Massabki, K. Petrecca, and F. Leblond, "Handheld macroscopic Raman spectroscopy imaging instrument for machine-learning-based molecular tissue margins characterization," *J. Biomed. Opt.* **26**, 1–18 (2021).
13. S. David, H. Tavera, T. Trang, F. Dallaire, F. Daoust, F. Tremblay, L. Richer, S. Meterissian, and F. Leblond, "Macroscopic inelastic scattering imaging using a hyperspectral line-scanning system identifies invasive breast cancer in lumpectomy and mastectomy specimens," *J. Biomed. Opt.* **under revi**, (2023).
14. K. Ember, F. Dallaire, A. Plante, G. Sheehy, M.-C. Guiot, R. Agarwal, R. Yadav, A. Douet, J. Selb, J. Tremblay, A. Dupuis, E. Marple, K. Urmey, C. Rizea, F. Leblond, C. G. Hadjipanayis, and K. Petrecca, "In Situ Brain Tumor Detection Using the Raman Spectroscopy Sentry System – Results of a Multicenter Study," *Nat. Commun.* **under revi**, (2023).
15. F. Leblond, F. Dallaire, T. Tran, R. Yadav, K. Aubertin, E. Goudie, P. Romeo, C. Kent, C. Leduc, and M. Liberman, "Subsecond lung cancer detection within a heterogeneous background of normal and benign tissue using single-point Raman spectroscopy," *J. Biomed. Opt.* **28**, 1–8 (2023).
16. S. David, A. Plante, F. Dallaire, J. P. Tremblay, G. Sheehy, E. Macdonald, L. Forrest, M. Daneshmand, D. Trudel, B. C. Wilson, L. Hopkins, S. Murugkar, B. Vanderhyden, and F. Leblond, "Multispectral label-free Raman spectroscopy can detect ovarian and endometrial cancer with high accuracy," *J. Biophotonics* **15**, 1–10 (2022).
17. G. Sheehy, F. Picot, F. Dallaire, K. Ember, T. Nguyen, K. Petrecca, D. Trudel, and F. Leblond, "Open-sourced Raman spectroscopy data processing package implementing a baseline removal algorithm validated from multiple datasets acquired in human tissue and biofluids," *J. Biomed. Opt.* **28**, 1–20 (2023).
18. K. Czamara, K. Majzner, M. Z. Pacia, K. Kochan, A. Kaczor, and M. Baranska, "Raman spectroscopy of lipids: a review," *J. Raman Spectrosc.* **46**, 4–20 (2015).
19. A. Rygula, K. Majzner, K. M. Marzec, A. Kaczor, M. Pilarczyk, and M. Baranska, "Raman spectroscopy of proteins: a review," *J. Raman Spectrosc.* **44**, 1061–1076 (2013).
20. A. C. S. Talari, Z. Movasaghi, S. Rehman, and I. U. Rehman, "Raman spectroscopy of biological tissues," *Appl. Spectrosc. Rev.* **50**, 46–111 (2015).
21. D. Wei, S. Chen, and Q. Liu, "Review of fluorescence suppression techniques in Raman spectroscopy," *Appl. Spectrosc. Rev.* (2015).
22. J. Zhao, H. Lui, D. I. Mclean, and H. Zeng, "Automated autofluorescence background subtraction algorithm for biomedical raman spectroscopy," *Appl. Spectrosc.* **61**, 1225–1232 (2007).